

Electronic Supplementary Information (ESI) for

All-in-one Hybrid Atmospheric Water Harvesting for All-day Water Production by Natural Sunlight and Radiative Cooling

Jiaying Xu¹, Xiangyan Huo¹, Taisen Yan¹, Pengfei Wang¹, Zhaoyuan Bai¹, Jingwei Chao¹, Ronggui Yang^{3,*}, Ruzhu Wang^{1,2,*}, Tingxian Li^{1,2,*}

¹ Institute of Refrigeration and Cryogenics, School of Mechanical Engineering, Shanghai Jiao Tong University, Shanghai 200240, China.

² Research Center of Solar Power & Refrigeration, Shanghai Jiao Tong University, Shanghai 200240, China.

³ School of Energy and Power Engineering, Huazhong University of Science and Technology, Wuhan 430074, China.

* Corresponding author. E-mail: Litx@sjtu.edu.cn (T. L.); Ronggui@hust.edu.cn (R. Y.); Rzwang@sjtu.edu.cn (R. W.).

Note S1. Theoretical models and prediction of sorption-based AWH (S-AWH) working capacity of composite sorbents under different water condensation temperatures.

Water capture (sorption) process of composite sorbents includes three steps (1): (i) chemisorption of water by anhydrous salt to be salt hydrates; (ii) deliquescence of salt hydrates to be saturated salt solution; (iii) water absorption of saturated salt solution to be dilute salt solution. Inversely, its water release (desorption) process also shows three steps, successively: (i) evaporation of water from dilute salt solution to saturated salt solution; (ii) crystallization in saturation salt solution to be solid salt hydrates; (iii) chemical desorption of salt hydrates to be salt anhydrites. Generally, the deliquescence of hygroscopic salts occurs at lower relative humidity (DRH) than ambient RH of arid regions; thus, the water sorption capacity of composite sorbent is high, contributed by all the above-mentioned three water sorption steps, whose water sorption capacity can be described by the following equation,

$$\omega = \alpha_{salt} \cdot \begin{cases} 0 & RH < CRH \\ \omega_{chem} & CRH \leq RH < DRH \\ \omega_{chem} + \omega_{deli} & RH = DRH \\ \omega_{chem} + \omega_{deli} + \omega_{ab} & RH > DRH \end{cases} \quad \text{Eq. S1}$$

where the α_{salt} means the salt content of composite sorbent. The ω_{chem} , ω_{deli} , and ω_{ab} represent the water sorption amount contributed by chemical sorption, deliquescence, and absorption of pure salts, respectively, wherein ω_{chem} and ω_{deli} are fixed values for specific salts. The CRH and DRH are the characteristic RH of chemical sorption and deliquescence, which can be found in literature or database. For pure LiCl, the values of ω_{chem} , ω_{deli} , CRH, and DRH are 0.43 g/g, 0.78 g/g, 2.7%, and 11.5%, at 25 °C respectively (2). It is worth mentioning that some hygroscopic salts have many coordinated water molecules, e.g., $\text{CaCl}_2 \cdot 6\text{H}_2\text{O}$ and $\text{MgCl}_2 \cdot 6\text{H}_2\text{O}$, showing a multi-step chemical desorption process and have several values of CRH, corresponding to different chemical desorption steps.

For the sorption capacity of solution absorption (ω_{ab}), it can be described and fitted with the D–A (Dubinin–Astakhov) equation (3),

$$\omega_{ab} = \omega_0 \exp(-x F^y) \quad \text{Eq. S2}$$

where the ω_0 , x , and y can be obtained by fitting the water sorption isotherms at the region of $RH > DRH$. The F represents the water sorption potential which is controlled by the RH and temperature according to the Polanyi potential theory (4).

$$F = -RT \ln(RH) \quad \text{Eq. S3}$$

The theoretical water sorption isotherms of pure LiCl are obtained according to Eq. S1-S3, as shown in Fig. S2. In comparison with water sorption isotherm at 25 °C, the isotherm of LiCl at 80 °C shows a higher CRH and lower DRH. A similar phenomenon was found in the water sorption isotherms of CaCl_2 (Fig. S3); moreover, the DRH becomes much lower that make the $\text{CaCl}_2 \cdot 2\text{H}_2\text{O}$ directly deliquesce to be saturated CaCl_2 solution at 80 °C, where the $\text{CaCl}_2 \cdot 4\text{H}_2\text{O}$ and $\text{CaCl}_2 \cdot 6\text{H}_2\text{O}$ no exist at this temperature.

Since the salts generally show negligible hysteresis for desorption after being confined inside a porous matrix, the working capacity of atmospheric water harvesting of composite sorbent can be determined by subtracting the equilibrium water content of sorbent under desorption condition from water sorption capacity under sorption

conditions, as following

$$\omega_{S-AWH} = \omega(T_{\text{sorp}}, RH_{\text{sorp}}) - \omega(T_{\text{de}}, RH_{\text{de}}) \quad \text{Eq. S4}$$

To show the influence of condensation temperature on water productivity, we make the following assumptions to calculate and show the influence of water condensation temperature on S-AWH capacity: (i) The solar collector is good enough to provide a stable heating temperature; (ii) The mass transfer resistance for water vapor flow from sorbent side to condenser side is small enough, and thus the water vapor pressure difference between these two sites can be ignored; (iii) The condensation resistance of condenser is small enough that the condensation pressure can be regarded as the saturated water vapor pressure at a local condensation temperature.

Based on the above assumptions, the water desorption pressure is the same as the water condensation pressure, controlled by the water condensation temperature. The water vapor pressure near sorbents (P_{de}) can be approximatively regarded as equal to the condensation pressure (P_{cond}), i.e., P_{de} equals the P_{cond} , then the RH_{de} can be described by condensation temperature and desorption temperature using the following equation.

$$RH_{\text{de}} = \frac{P_{\text{sat}}(T_{\text{cond}})}{P_{\text{sat}}(T_{\text{de}})} = \frac{\exp\left(\frac{17.27 T_{\text{cond}}}{237.3 + T_{\text{cond}}}\right)}{\exp\left(\frac{17.27 T_{\text{de}}}{237.3 + T_{\text{de}}}\right)} \quad \text{Eq. S5}$$

If we set the T_{sorption} and RH_{sorption} at 25 °C and 30%, as a typical ambient condition at arid regions and set the T_{de} at 80 °C, we can get the relationship between condensation temperature and S-AWH capacity for various composite sorbents with different salt contents according to Eq. S1-S5.

Considering the sorption temperature (T_{sorp}) and sorption RH (RH_{sorp}) are generally equal to that of ambient air during the water capture process and the desorption temperature (T_{de}) are determined by the solar irradiation intensity and thermal insulation condition for solar-driven S-AWH device, the RH of air near sorbent during water desorption process (RH_{de}) is one of most efficient matter dominating the AWH capacity. For example, if the RH_{de} is higher than the DRH at desorption temperature, the liquid salt solution will not transfer to solid crystals, resulting in a much lower AWH capacity.

Note S2. Thermal analysis of the energy flux for a typical passive air-cooling solar-driven S-AWH device

In many reported S-AWH devices (5-7), the materials with all-spectra high absorbance characters were used to realize a high solar absorbance above 95%. However, it also brings a large heat loss through thermal radiation if using an all-spectra high transmittivity cover, such as PE membrane (Fig. S5) (8).

The net heat loss through thermal radiation ($P_{\text{net,rad}}$) can be calculated by subtracting the input radiation of the atmosphere (P_{atm}) from the total radiation of the solar absorber ($P_{\text{rad,ab}}$), as described by the following equation,

$$P_{\text{net,rad}} = P_{\text{rad,ab}} - P_{\text{atm}} \quad \text{Eq. S6}$$

where the $P_{\text{net,rad}}$ can be obtained by following Eq. S7 and a simplified Eq. S8 if we ignore the influence of zenith angle (ϑ) and azimuth angle (φ).

$$P_{\text{rad,ab}}(T) = \int_0^\infty \int_0^{2\pi} \int_0^{\pi/2} \varepsilon_{\text{ab}}(\lambda, \theta, \varphi, T) I_{\text{BB}}(\lambda, T) \cos\theta \cdot \sin\theta \cdot d\theta d\varphi d\lambda \quad \text{Eq. S7}$$

$$P_{\text{rad}}(T) = \pi \int_0^\infty \varepsilon(\lambda) I_{\text{BB}}(\lambda, T) d\lambda \quad \text{Eq. S8}$$

The I_{BB} represents the spectral radiated power of blackbody, described by the following equation.

$$I_{\text{BB}}(\lambda, T) = \frac{2h_0c_0^2}{\lambda^5 e^{h_0c_0/(\lambda k_0T)} - 1} \quad \text{Eq. S9}$$

If we assume the solar absorber has a high working performance of 95% absorbance at all spectra ranges. The calculation of P_{atm} is shown in the following section. Then, we found that although a very small amount of solar energy was lost by reflectance (50 W/m²), a huge amount of heat was lost through radiation (481 W/m²) at a typical solar collection temperature of 80 °C. Since the PE cover is all-spectra high transmittivity and thus cannot provide effective cooling power, whose thermal balance can be reached when the internal natural heat convection from the solar absorber equals the external natural heat convection if we ignore the small contribution of thermal conduction, as described by the following equation,

$$h_{\text{external}}(T_{\text{PE}} - T_{\text{amb}}) = h_{\text{internal}}(T_{\text{ab}} - T_{\text{PE}}) \quad \text{Eq. S10}$$

where the natural heat convection coefficient of external air (h_{external}) and internal air (h_{internal}) are determined as 10.8 W/(m²·K) and 2.2 W/(m²·K) according to the natural heat convection experience equations. Accordingly, the temperature of PE (T_{PE}) can be estimated as 38 °C at the assumption of the ambient temperature at 30 °C and solar absorber temperature at 80 °C. This high condensation temperature cannot drive the complete water condensation and needs an extra heat sink, as reported in the literature. A very low theoretical thermal efficiency of 16% was determined, ascribing to the large amount of heat losses through convection and radiation. Besides, the operation of such air-cooling solar-driven S-AWH devices highly relies on a heavy, bulky, or energy-intensive condenser. Consequently, it is urgent to improve the thermal design and condenser, realizing a more efficient passive S-AWH.

Note S3. Thermal analysis of energy flux for novel passive radiative cooling-assisted solar-driven all-in-one S-AWH device

Although the radiative cooling membrane (PDMS) provides a cooling power by harvesting cold from the universe, it also brings some extra energy absorbance or input such as the solar absorption of the condensed water on the membrane, and the radiative heat transfer from solar absorber (Fig. S6).

Therefore, it is necessary to figure out whether a net cooling power can be provided by a radiative cooling membrane, as described by the following equation,

$$P_{\text{net,cond}} = P_{\text{rad,PDMS}} - P_{\text{atm}} - \alpha_{\text{PDMS}}P_{\text{solar}} - \alpha_{\text{water}}P_{\text{solar}} - P_{\text{net,rad,ab}} - P_{\text{nonrad}} \quad \text{Eq. S11}$$

where the α_{PDMS} and α_{water} present the absorbances of solar energy for PDMS and pure water. The contributed cooling power from total radiative cooling of PDMS can be described by the following equation,

$$P_{\text{rad,PDMS}}(T) = \int_0^\infty \int_0^{2\pi} \int_0^{\pi/2} \varepsilon_{\text{PDMS}}(\lambda, \theta, \varphi, T) I_{\text{BB}}(\lambda, T) \cos\theta \cdot \sin\theta \cdot d\theta d\varphi d\lambda \quad \text{Eq. S12}$$

where $\varepsilon_{\text{PDMS}}(\lambda, \vartheta, \varphi, T)$ and $I_{\text{BB}}(T, \lambda)$ are the angle-dependent emissivities of the PDMS and the spectral irradiance of a blackbody (unit: $\text{W/m}^2 \cdot \text{sr} \cdot \text{nm}$) at radiative temperature (T), wherein the λ , ϑ , and φ represent wavelength, zenith angle, and azimuth angle, respectively. For mainly practical surfaces, the influence of azimuth angle (φ) can be ignored. Since the PDMS shows an approximately omnidirectional thermal emission (9), the influence of the zenith angle (ϑ) was also ignored in this study. Thus, the total radiative cooling power can be simplified as,

$$P_{\text{rad,PDMS}}(T) = \pi \int_0^\infty \varepsilon_{\text{PDMS}}(\lambda) I_{\text{BB}}(\lambda, T) d\lambda \quad \text{Eq. S13}$$

Apart from emitting energy to the universe, the PDMS and the condensed water also absorb heat from the atmosphere (P_{atm}) and solar energy (P_{solar}), and have heat exchange with ambient air if there is a temperature difference between condensation temperature and ambient temperature (P_{nonrad}).

Different from the PDMS, the atmosphere shows a different emissivity at different angles, modeled by

$$\varepsilon_{\text{atm}}(\lambda, \theta) = 1 - [\tau_{\text{atm}}(\lambda, 0)]^{1/\cos\theta} \quad \text{Eq. S14}$$

where the τ_{atm} presents the vertical transmittance of the atmosphere, whose data can be found in literature (10). Then, the atmospheric radiation absorbed by PDMS can be described by

$$P_{\text{atm}} = 2\pi \int_0^\infty \int_0^{\pi/2} \alpha_{\text{PDMS}}(\lambda) \varepsilon_{\text{atm}}(\lambda, \theta) I_{\text{BB}}(\lambda, T_{\text{atm}}) \cos\theta \sin\theta d\theta d\lambda \quad \text{Eq. S15}$$

Considering the measured results of absorbance of the PDMS and reported emissivity of the atmosphere are both discrete data points, Eq. S15 is converted to a numerical trapezoid summation formula,

$$P_{\text{atm}} = 2\pi \sum_{\theta=0}^{\theta=\pi/2} \sum_{\lambda=0.2 \mu\text{m}}^{\lambda=20 \mu\text{m}} \frac{(\theta_{i+1}-\theta_i)(\lambda_{i+1}-\lambda_i)}{4} (f(\theta_i, \lambda_i) + f(\theta_{i+1}, \lambda_i) + f(\theta_i, \lambda_{i+1}) + f(\theta_{i+1}, \lambda_{i+1})) \quad \text{Eq. S16}$$

where the function $f(\vartheta, \lambda)$ is the integrated function in Eq. S15. For the radiative heat transfer between the radiative cooling membrane and solar absorber ($P_{net,rad,ab}$), its net heat transfer power can be described by

$$P_{net,rad,ab} = \pi \int_0^\infty \varepsilon_{ab}(\lambda) \alpha_{PDMS}(\lambda) I_{BB}(\lambda, T_{ab}) d\lambda - \pi \int_0^\infty \varepsilon_{PDMS}(\lambda) \alpha_{ab}(\lambda) I_{BB}(\lambda, T_{PDMS}) d\lambda \quad \text{Eq. S17}$$

To weaken the heat transfer from the solar absorber to the radiative cooler, we chose the selective solar absorber panel (cermet-coated aluminum) as sun light-to-heat collector. The solar absorber has high sunlight absorbance but has low heat emittance, whose spectra property was characterized, as shown in Fig.S7.

For the non-radiative heat transfer caused by the temperature difference, the heat transfer power can be described by

$$P_{nonrad} = h_{external}(T_{amb} - T_{PDMS}) + h_{internal}(T_{ab} - T_{PDMS}) \quad \text{Eq. S18}$$

which contains the heat convection between PDMS and ambient air and the heat convection between PDMS and hot solar absorber. The heat transfer through thermal conduction was ignored as a result of the low thermal conductivity of air. According to the above models, the net radiative cooling by PDMS was found very low, indicating the amount of heat input is too large that consume all the cooling power. To realize an effective output of cooling power for water condensation, the loss of cooling power must be weakened by reducing the heat of P_{atm} , $\alpha_{water}P_{solar}$, $P_{net,rad,ab}$ and P_{nonrad} , which contribute to the major four heat inputs. Considering the atmosphere emits major heat at the zenith angle ranging above 60° (Fig. S8), part of the emitted heat can be eliminated by adding a radiation shield.

However, adding a radiation shield also limits the radiative cooling power of PDMS by blocking the radiation from PDMS. To reduce the P_{atm} and meanwhile not harm to reducing P_{rad} , Haechler et al. recently reported using a special shield with high reflectance at the infrared band and well-optimized shape to eliminate part of P_{atm} (11). The solar absorbance by condensed water, $\alpha_{water}P_{solar}$, can be reduced by timely removing water droplets or maintaining a thin water film, keeping a low absorbance of water. The radiative heat transfer from the solar absorber to PDMS, $P_{net,rad,ab}$, can be sharply reduced by using a selective solar absorber whose emittance at the infrared range is very low. For reducing the cold loss by convection, P_{nonrad} , well thermal insulation between the radiative cooling membrane and solar absorber is considered.

According to the above thermal design guidelines, a theoretical maximum condensation power by PDMS of 181 W/m^2 at 30°C can be realized for this RC-assisted S-AWH system, at the assumption of atmospheric radiation (P_{atm}) were reduced by 20%, absorbed solar energy by water ($\alpha_{water}P_{solar}$) and the radiative heating power from solar absorber ($P_{net,rad,ab}$) were apparently weakened to a low value, and the convection heat was eliminated by advanced engineering design.

Note S4. Evaluation and comparison of condensation efficiency by using air cooling and radiative cooling.

The current condensation of AWH generally uses a natural air-cooling strategy enabled by the finned radiator. The cooling power of the finned air condenser can be improved by enlarging the heat-exchange area or increasing forced airflow; however, the enhanced performance relies on heavy metal fins, bulky space, and extra energy consumption by air fans. Considering that a compact and light AWH device is the design goal of portable water harvesting, we propose here three indexes to evaluate the efficiency of the condenser (EOC) in perspective of surface area, mass, and volume, respectively, as follows,

$$EOC_{\text{area}} = \frac{q_{\text{cond}}}{A_{\text{cond}}(T_{\text{cond}} - T_{\text{amb}})} \quad \text{Eq. S19}$$

$$EOC_{\text{mass}} = \frac{q_{\text{cond}}}{m_{\text{cond}}(T_{\text{cond}} - T_{\text{amb}})} \quad \text{Eq. S20}$$

$$EOC_{\text{volume}} = \frac{q_{\text{cond}}}{V_{\text{cond}}(T_{\text{cond}} - T_{\text{amb}})} \quad \text{Eq. S21}$$

where the A_{cond} , m_{cond} , and the V_{cond} represent the surface area, mass, and volume of the condenser for S-AWH, respectively. Here, the q_{cond} is the cooling power (W) provided by the condenser, which is determined by the water production rate ($\dot{\omega}$, $\text{g}_{\text{water}} \text{ s}^{-1}$) of the S-AWH system, as described by the following,

$$q_{\text{cond}} = \dot{\omega} \Delta H_{\text{cond}} \quad \text{Eq. S22}$$

where the ΔH_{cond} represents the enthalpy of water condensation.

For portable S-AWH devices, the desirable occupied area, mass, and volume of the condenser are roughly estimated as 0.5 m^2 , 10 kg, and 30 L for one person, respectively. Assuming the daily water consumption (including food sources) of 3.7 L for one adult man (12), we give here the design targets of EOCs for portable S-AWH devices under the common heat-exchange temperature of 5 °C. The EOC_{area} , EOC_{mass} , and EOC_{volume} should be kept above 128.4 $\text{W m}^{-2} \text{ K}^{-1}$, 6.5 $\text{W kg}^{-1} \text{ K}^{-1}$, and 2140.5 $\text{W m}^{-3} \text{ K}^{-1}$, respectively. Apparently, natural air-cooling cannot provide enough cooling power for a compact portable S-AWH device and forced air-cooling can be introduced, but at the expense of extra energy consumption (Table S1) (13, 14).

The radiative-cooling condenser exhibits distinct superiorities on lowering the mass and the volume. Although it has relatively low cooling power per condensation surface area, it does not rely on a heavy and bulk metal heat exchanger. Most excitingly, realizing a compact all-in-one hybrid AWH device becomes feasible by rational thermal design using a radiative-cooling condenser with a transparent radiative cooling membrane. In this work, the PDMS-PET radiative cooler, solar thermal absorber, and water sorbent sheet are layer-by-layer assembled from the top to the bottom in the hybrid AWH device with the same physical areas. Consequently, impressive water productivity and high energy efficiency were achieved, as shown in Fig.5F and following Table S2.

The thermal energy efficiency (η_{thermal}) is calculated according to the collected or desorbed water, according to the following equation

$$\eta_{\text{thermal}} = \frac{m_{\text{water}} \Delta H_{\text{water}}}{Q_{\text{in}}} \quad \text{Eq. S23}$$

where the m_{water} represents the mass of collected or desorbed water, the ΔH_{water} is the enthalpy (latent heat) of water condensation, and the Q_{in} is the input energy. For solar-driven atmospheric water harvesting, the Q_{in} means the input solar irradiation.

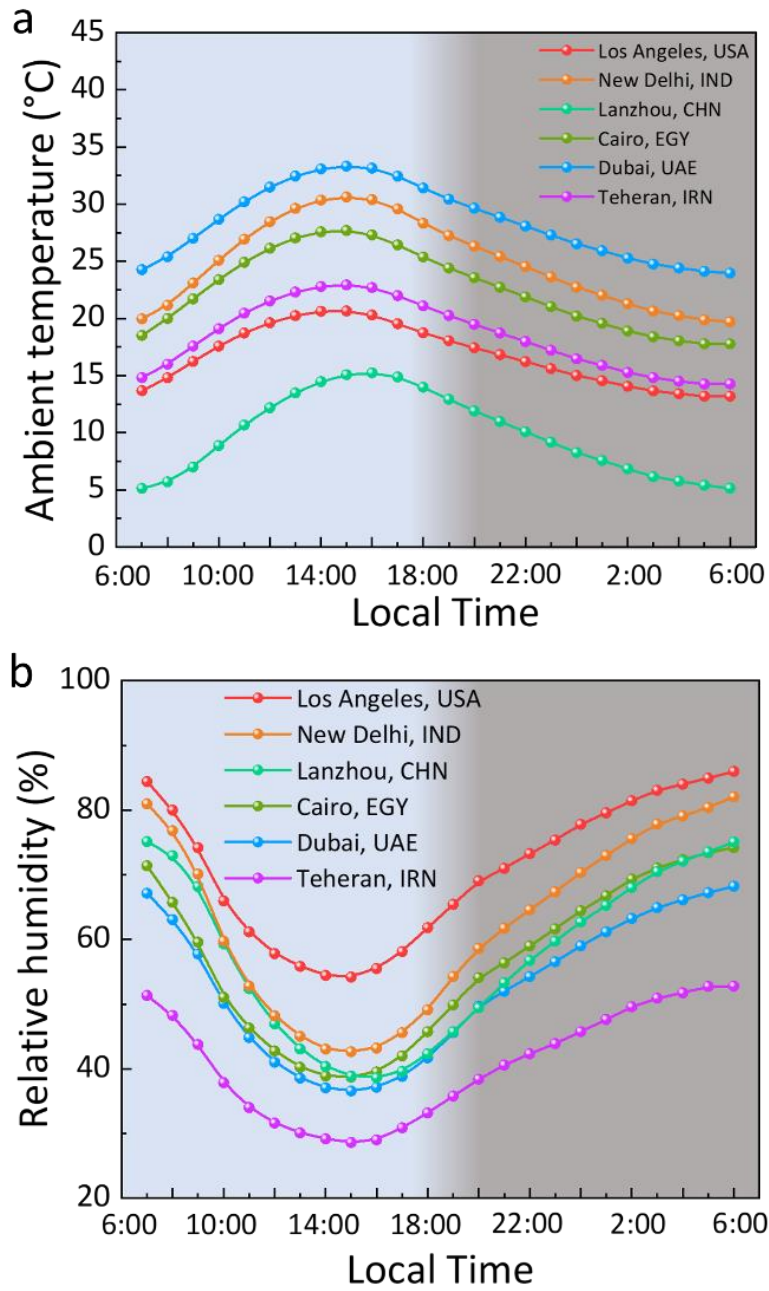


Figure S1. The evolution of the average climate conditions of typical cities located in arid or semi-arid regions, including Dubai in the United Arab Emirates, New Delhi in India, Cairo in Egypt, Los Angeles in America, Teheran in Iran, and Lanzhou in China. a, Temperature. b, Relative humidity. Data come from Meteonorm.

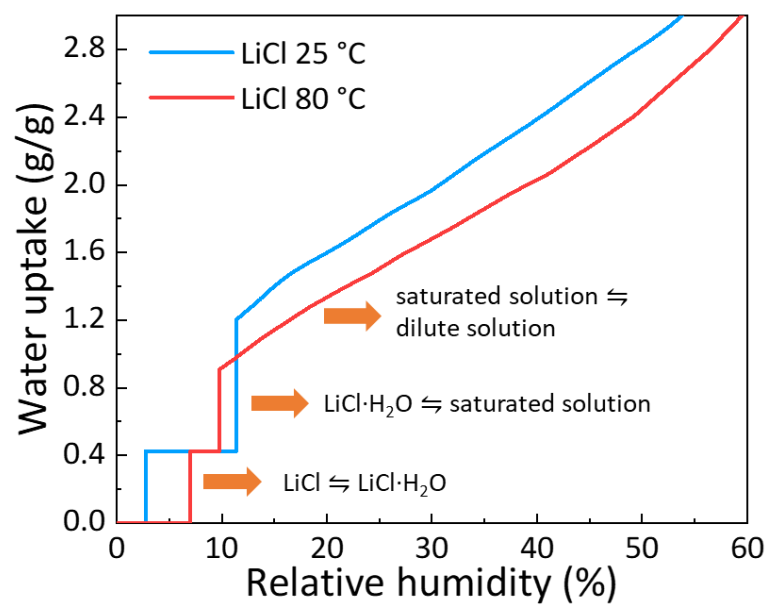


Figure S2. Theoretical water sorption isotherms of pure LiCl at 25 °C and 80 °C, respectively.

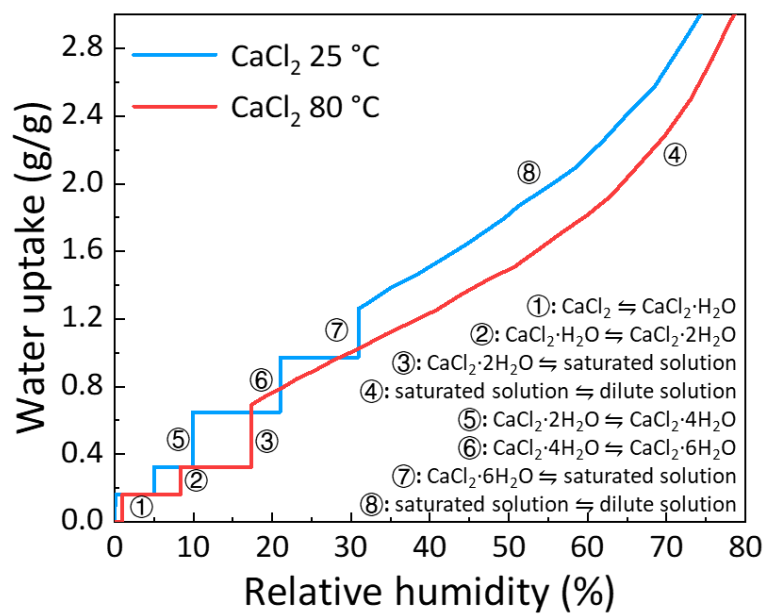


Figure S3. Theoretical water sorption isotherms of pure CaCl₂ at 25 °C and 80 °C, respectively.

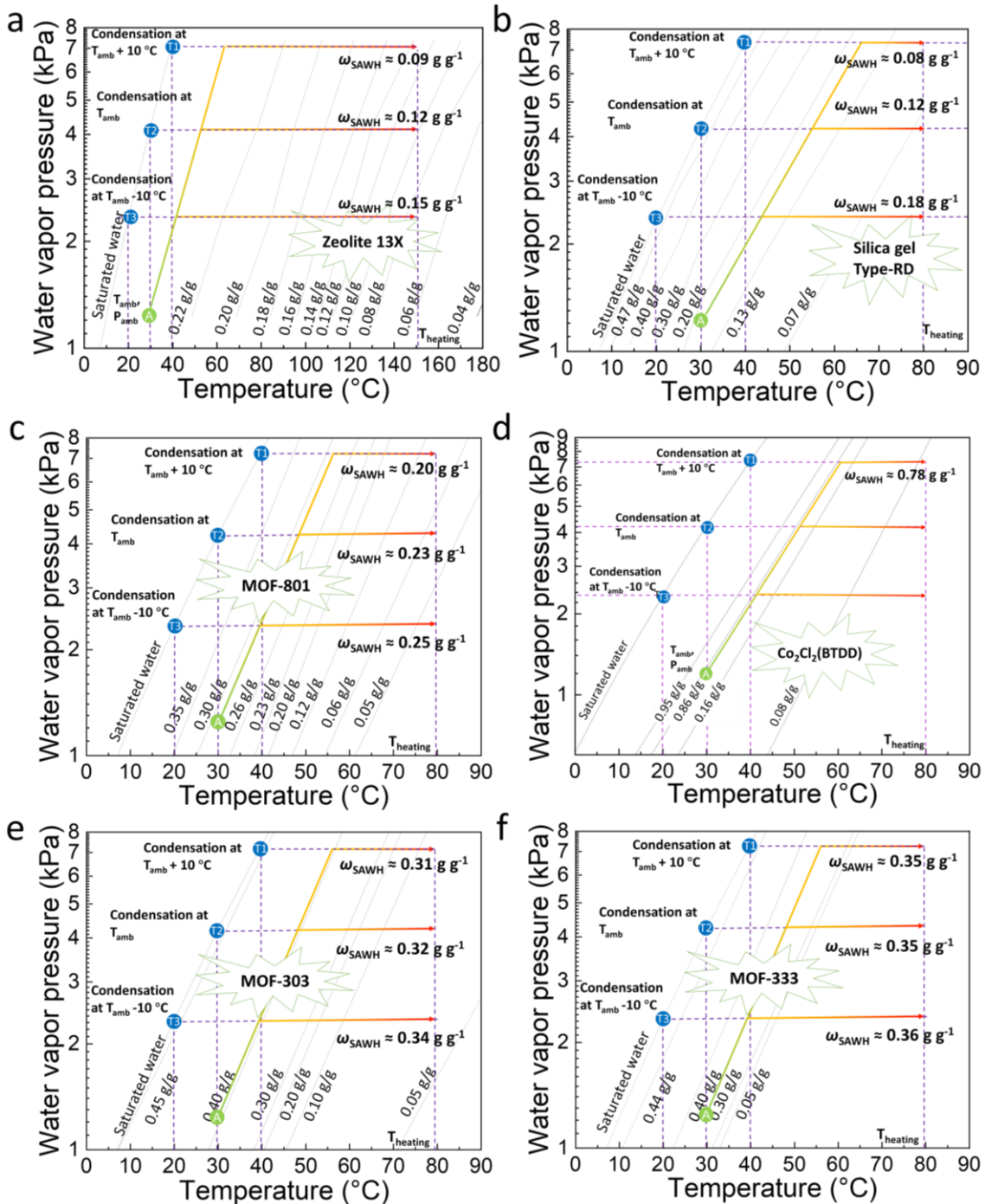


Figure S4. Water sorption equilibrium characteristics of typical sorbents for S-AWH. a, zeolite 13X. b, silica gel Type-RD. c, MOF-801. d, $\text{Co}_2\text{Cl}_2(\text{BTDD})$. e, MOF-303. f, MOF-333. The sorption equilibrium curves of typical sorbents are obtained according to the reported water sorption isothermal curves at different temperatures or water sorption isobaric curves at different vapor pressures (15-20).

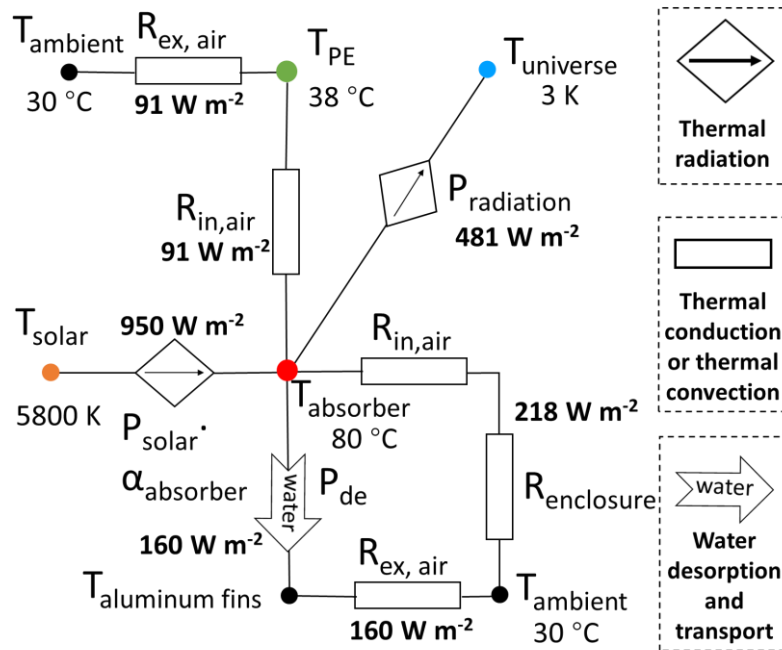


Figure S5. The thermal resistance and heat capacity network of a typical air-cooling passive S-AWH prototype. The capacitance symbol represents the heat consumption by sensible heat of heat capacity. The resistance symbol represents the thermal resistance of heat convection or conduction. The diamonds-shaped symbol represents the heat transfer through heat radiation.

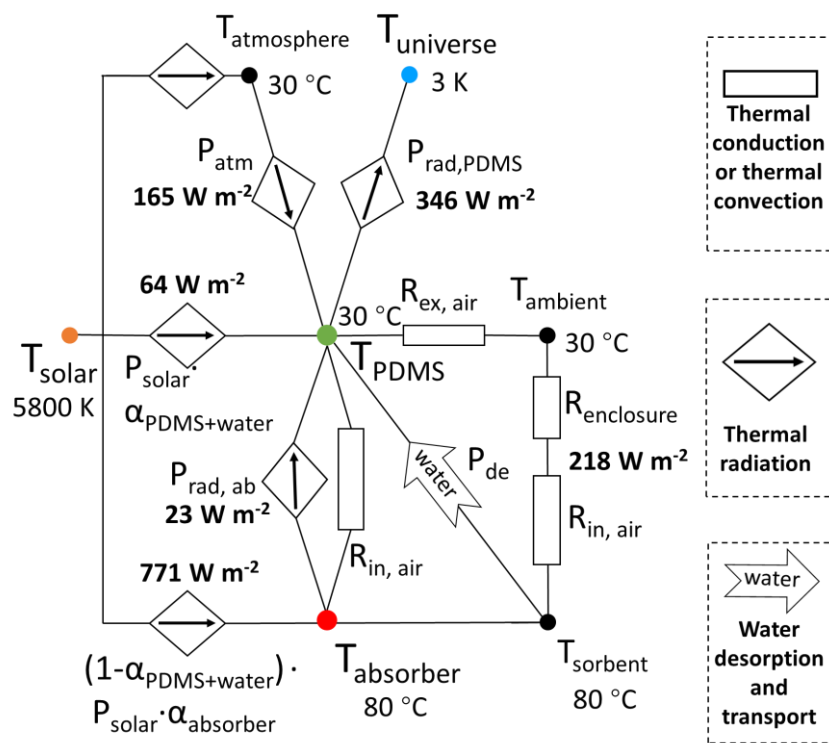


Figure S6. Thermal resistance and heat capacity network of the all-in-one hybrid AWH prototype. The capacitance symbol represents the heat consumption by sensible heat of heat capacity. The resistance symbol represents the thermal resistance of heat convection or conduction. The diamonds-shaped symbol represents the heat transfer through heat radiation.

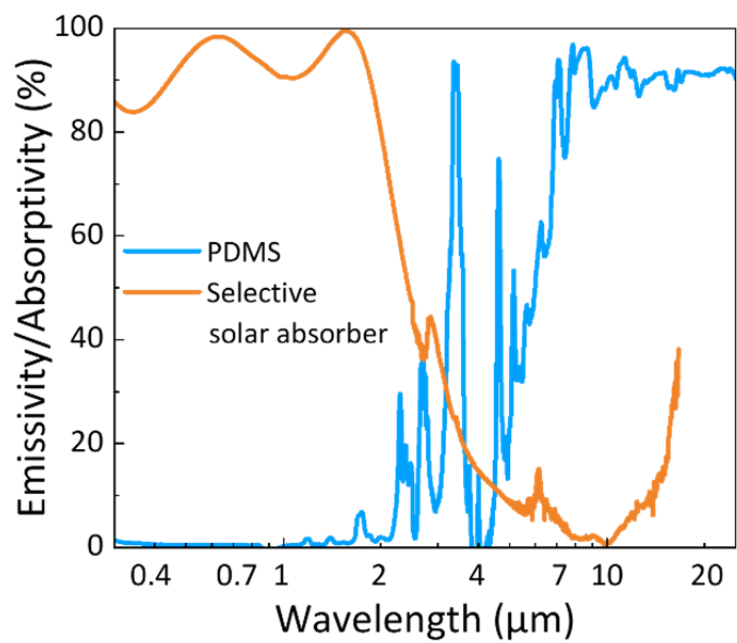


Figure S7. Spectral characters of PDMS membrane and selective solar absorber.

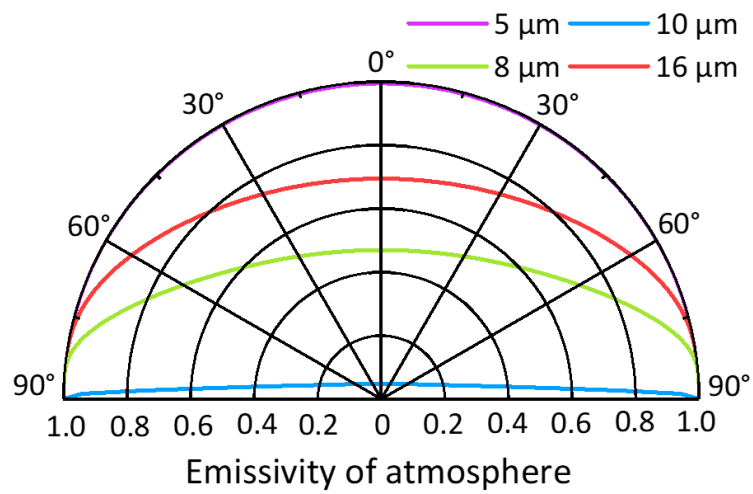


Figure S8. The modeled angle-dependent atmospheric emissivity distributions at the wavelengths of 5 μm , 10 μm , 8 μm , and 16 μm , respectively.

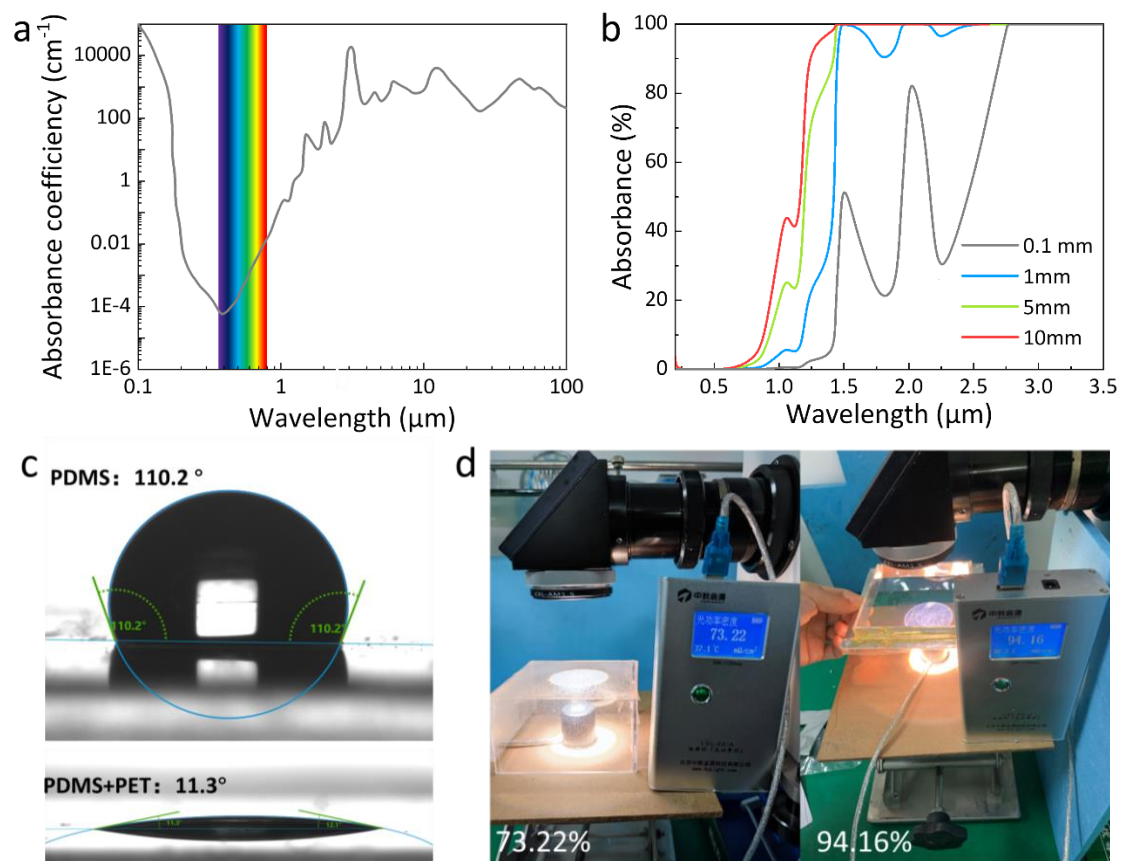


Figure S9. Spectral characteristics of water and enhancing solar transmittance by employing super hydrophilic membrane. a, The absorbance coefficient (A) of pure water. b, The absorbance of pure water at vis-NIR band. The relative absorbance was calculated by $1 - \text{Transmittance (T)}$, and the transmittance was calculated by the equation of $A = \log_{10}(1/T)$. c, Contact angles of PDMS membrane and PDMS-PET membrane with water droplets. d, The sunlight transmittance of water condensed on the PDMS membrane and water condensed on the PDMS-PET membrane under standard one sun irradiation.

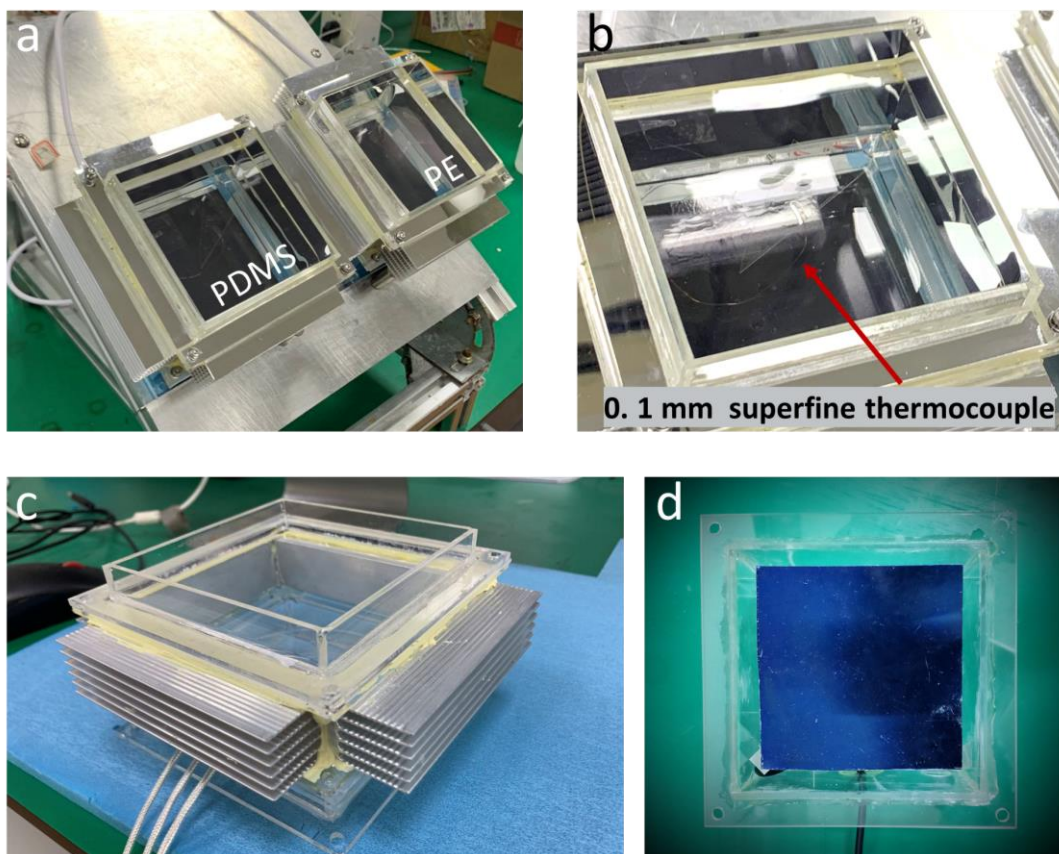


Figure S10. Optical photos of the atmospheric water harvesting device. a, all-in-one hybrid AWH devices of the PDMS group and PE group. The aluminum fins are covered by aluminum foil to reduce the input solar heat. b, 0.1 mm superfine thermocouple for measuring the temperature of the membrane. c, Four aluminum plate-fin heat sinks for covering part of condensation heat. The device was sealed by glue. d, The commercial 8.5 cm*8.5 cm selective solar absorber. e, the composite sorbent adhered to the back side of the selective solar absorber. The thickness of the sorbent was selected as 1 cm for achieving a large absolute amount of collected water. f, Two weighting sensors for measuring the mass change of sorbents during the water collection process.

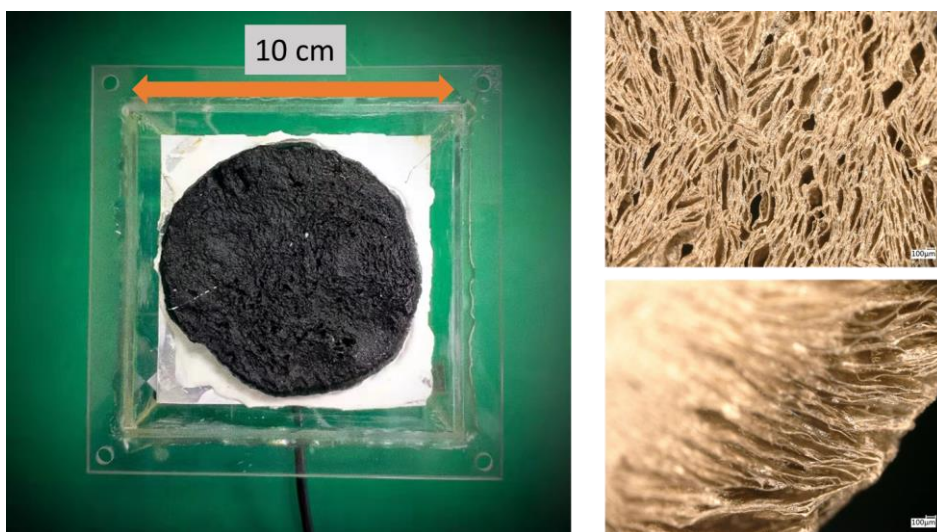


Figure S11. Photos of the composite sorbent adhered on the back side of the selective solar absorber. The thickness of the sorbent was selected as 1 cm for achieving a large absolute amount of collected water.

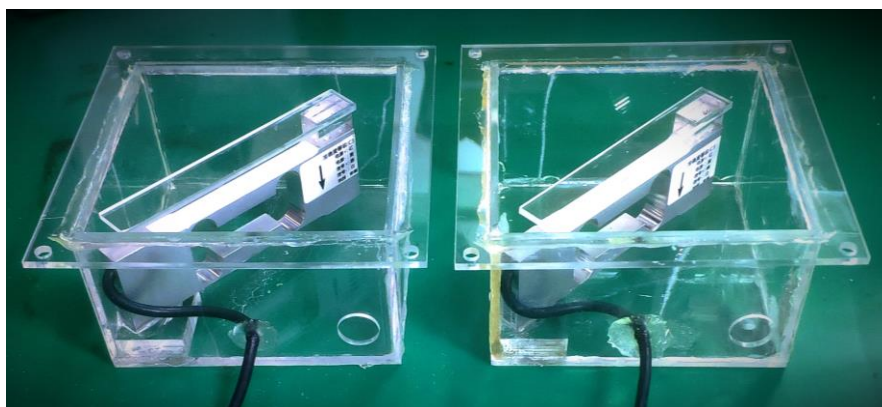


Figure S12. Photo of two weighing sensors for measuring the mass change of sorbents during the water collection process.

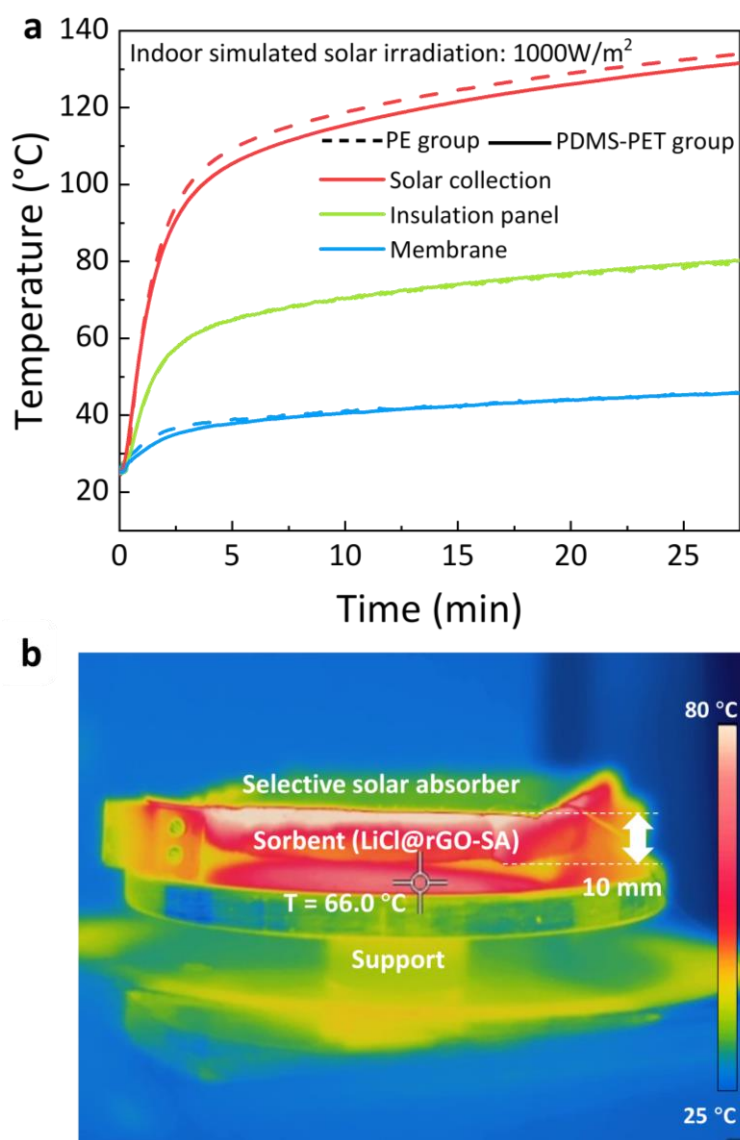


Figure S13. Temperature profiles under indoor experiments and water sorption capacity comparison of the state-of-the-art sorbents. a, Temperature profiles of the selective solar absorber, insulation panel, and PDMS-PET TRC membrane under indoor experiments without installing sorbent. The dotted lines are temperature profiles of the selective solar absorber, insulation panel, and PE membrane of the PE group. b, IR image showing the temperature distribution of LiCl@rGO-SA exposed under one standard sun irradiation, provided by the solar simulator of UHE-NS-100 (Sciencetech, Canada, with high accuracy of Class AAA).

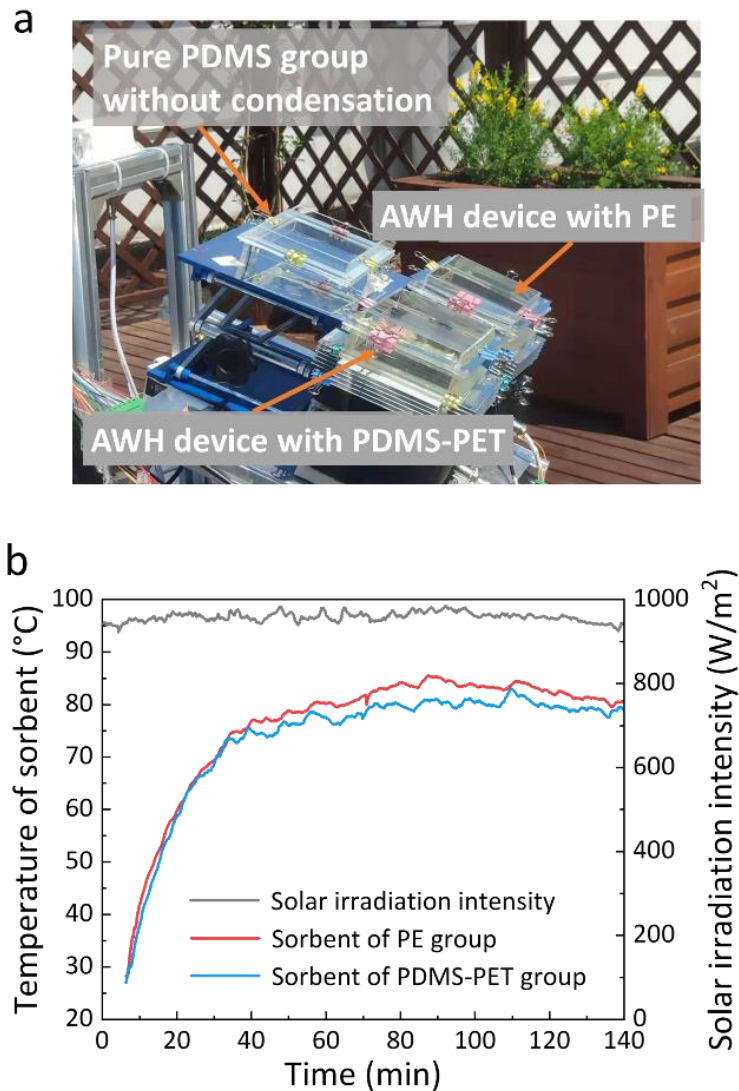


Figure S14. Outdoor daytime sunlight-driven sorption-based AWH (S-AWH). a, Photos showing three AWH devices during the outdoor experimental demonstration. An extra pure PDMS group without water condensation and thermal insulation was set to show the net daytime radiative cooling power for PDMS without condensation. b, Solar irradiation intensity of natural sunlight on May 1, 2021, in Shanghai, China, together with the temperature profiles of sorbents in the all-in-one hybrid AWH devices with/without radiative cooling.

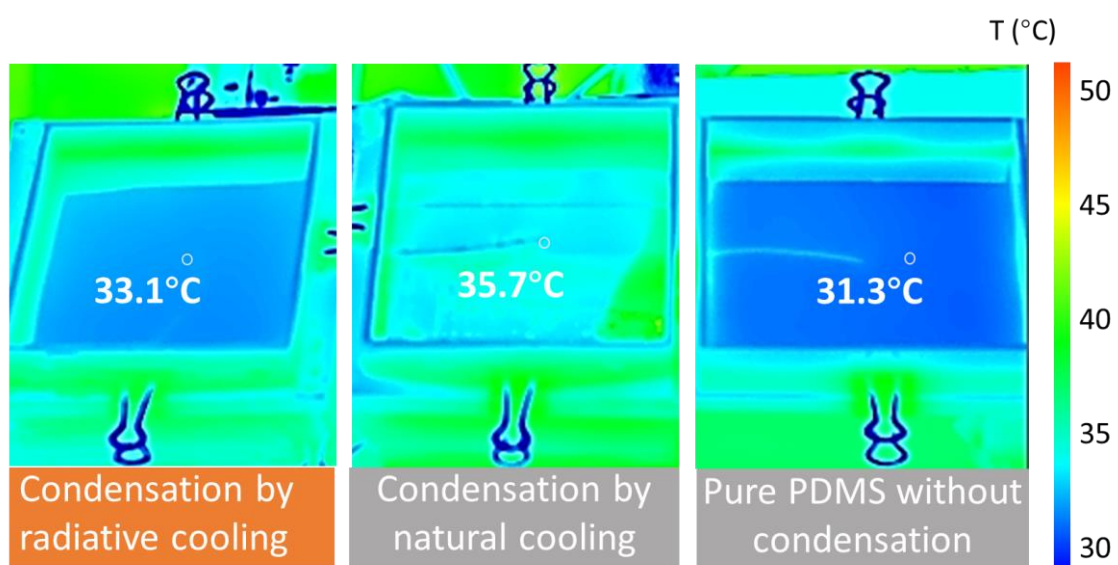


Figure S15. Infrared temperature mapping shows the temperature evolutions of three devices during the water condensation-collection process. The first is the AWH device with radiative-cooling-assistant condenser, the second is the AWH device without radiative cooling effects, and the third is the pure PDMS membrane without water condensation as the comparison group.

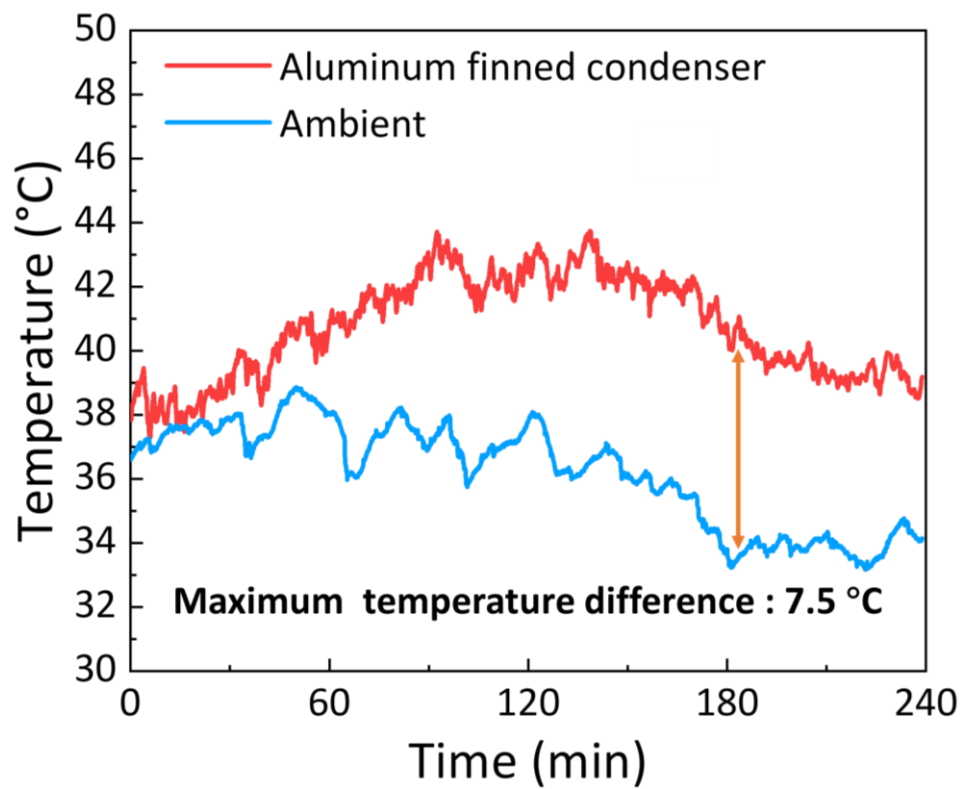


Figure S16. Temperature profiles of the aluminum finned condenser and ambient air during the S-AWH process, measured on Jun. 22, 2021.

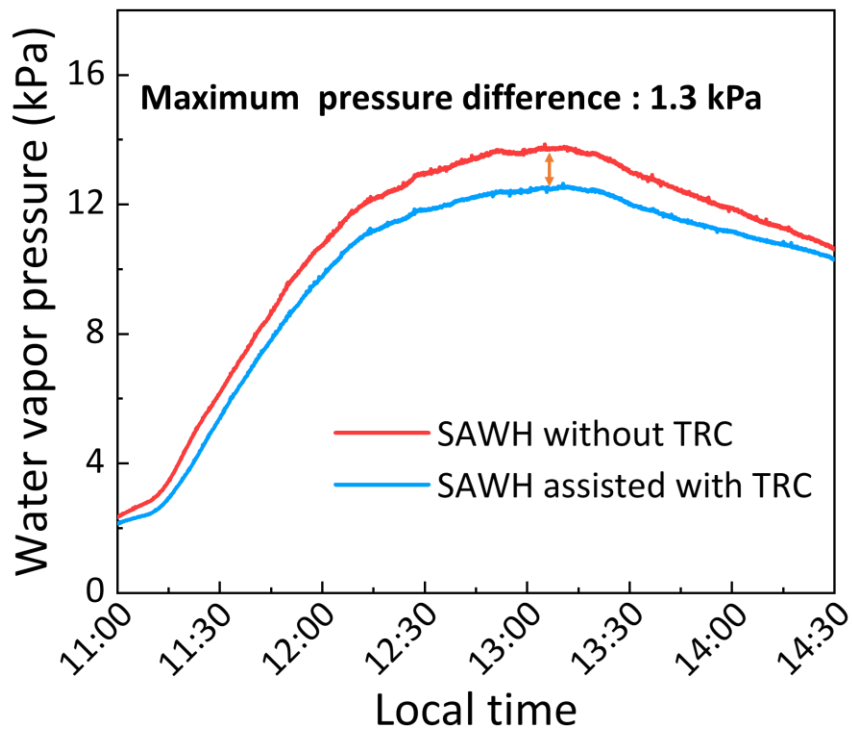


Figure S17. Water vapor pressure profiles in the two hybrid AWH devices. The low condensation temperature provided by radiative cooling enables a low water vapor pressure inside the AWH chamber, making the water release more deep and fast.

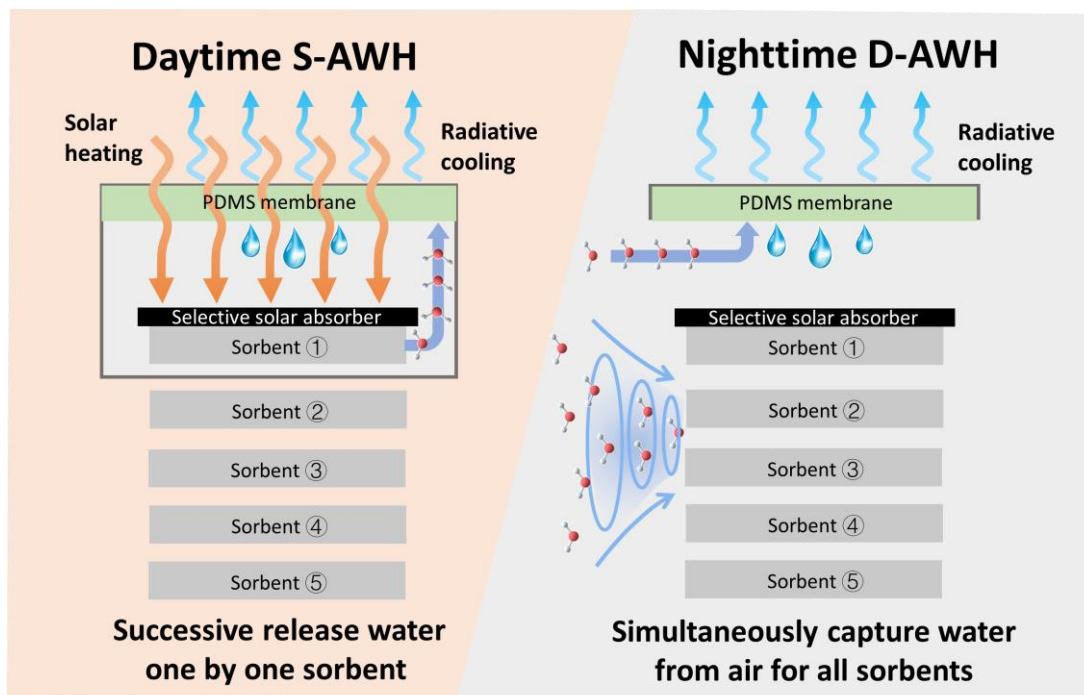
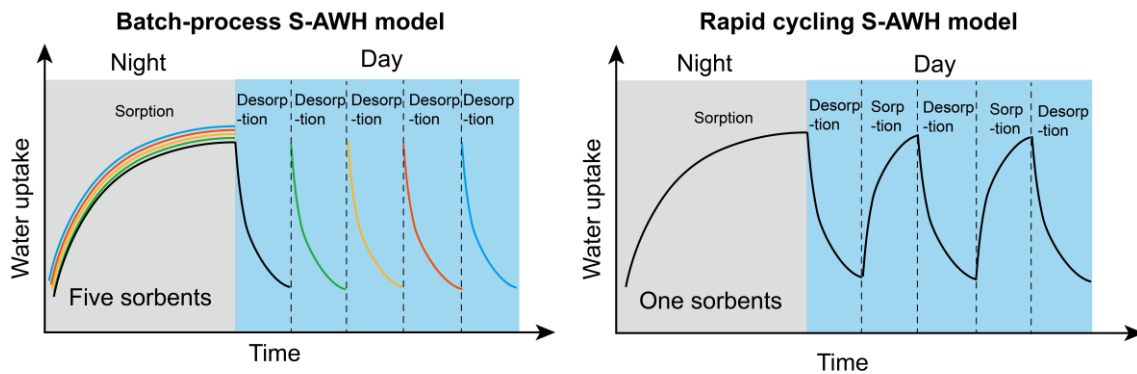


Figure S18. Continuously operation process of the all-in-one hybrid AWH device with five pieces of sorbents. All the sorbents vertically packed perform water sorption from ambient air simultaneously in the nighttime and then undergo water desorption successively under solar heating for water harvesting in the daytime by putting sorbents inside the heating chamber one by one.



Assumptions:

Each sorbent with same water uptake capacity: w_0 (g g⁻¹)

Each dry sorbent with same mass: m_0 (g)

AWH device with solar heating area: A (m²)

Working based on batch-process strategy

Water productivity per mass of sorbent:

$$SAWH_{\text{mass}} = w_0$$

Water productivity per solar heating area:

$$SAWH_{\text{area}} = \frac{5w_0m_0}{A}$$

Working based on rapid-cycling strategy

Water productivity per mass of sorbent:

$$SAWH_{\text{mass}} = 3w_0$$

Water productivity per solar heating area:

$$SAWH_{\text{area}} = \frac{3w_0m_0}{A}$$

Figure S19. Schematic showing the water productivity difference between S-AWH based on batch-process strategy and rapid-cycling strategy.

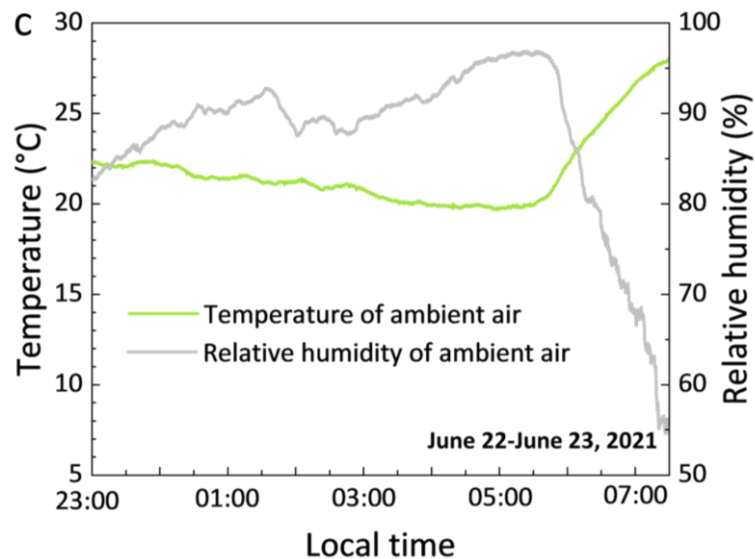
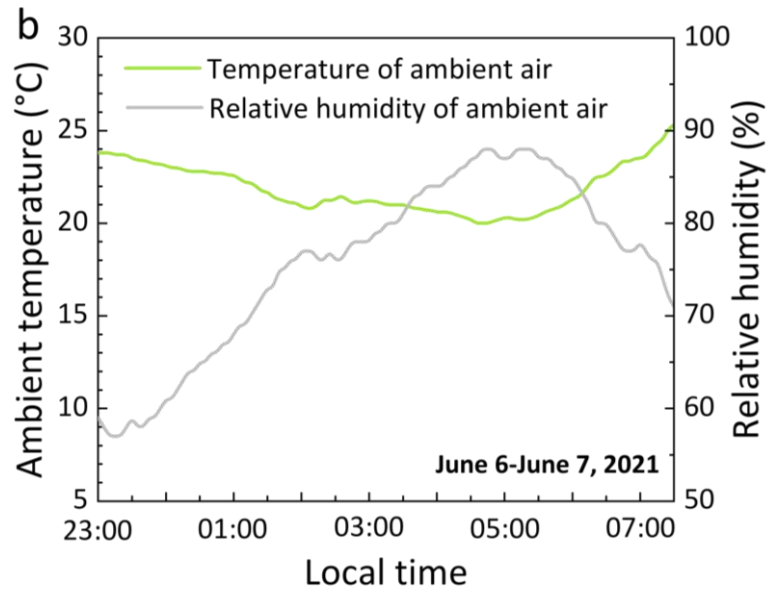
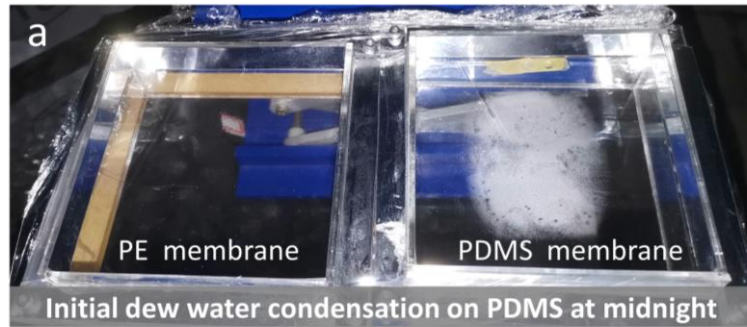
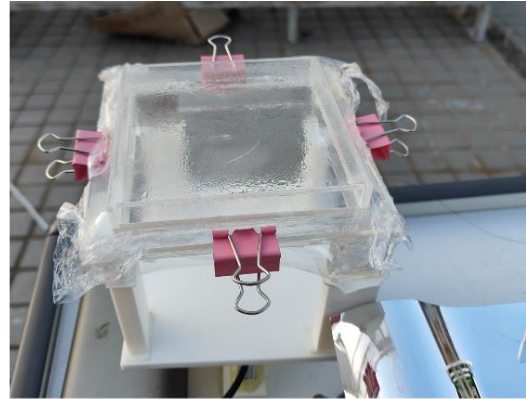


Figure S20. Outdoor nighttime radiative cooling-driven direct dew-based AWH (D-AWH). a, Photo of water harvesting devices using PE and PDMS membrane at the initial phase of dew water condensation at midnight. Only water droplets are found on the back side of the PDMS membrane. These two devices are covered by top convective covers to reduce the heat transfer by air convection. b, Temperature and humidity evolutions of ambient air during the D-AWH demonstration, measured on Jun. 6, 2021. c, Temperature and humidity evolutions of ambient air during the D-AWH demonstration, measured on Jun. 22, 2021.



Outdoor SAWH demonstration, photo taken on the morning of March 7, 2024.



Outdoor DAWH demonstration, photo taken on the dawn of March 8, 2024.

Figure S21. Photos showing the SAWH and DAWH in the arid region on the same day. The outdoor experiments were conducted on Mar. 7, 2024, on the roof of the Key Laboratory of Solar Heating and Cooling Technology of Yunnan Provincial Universities, Yunnan Normal University, Kunming, China.

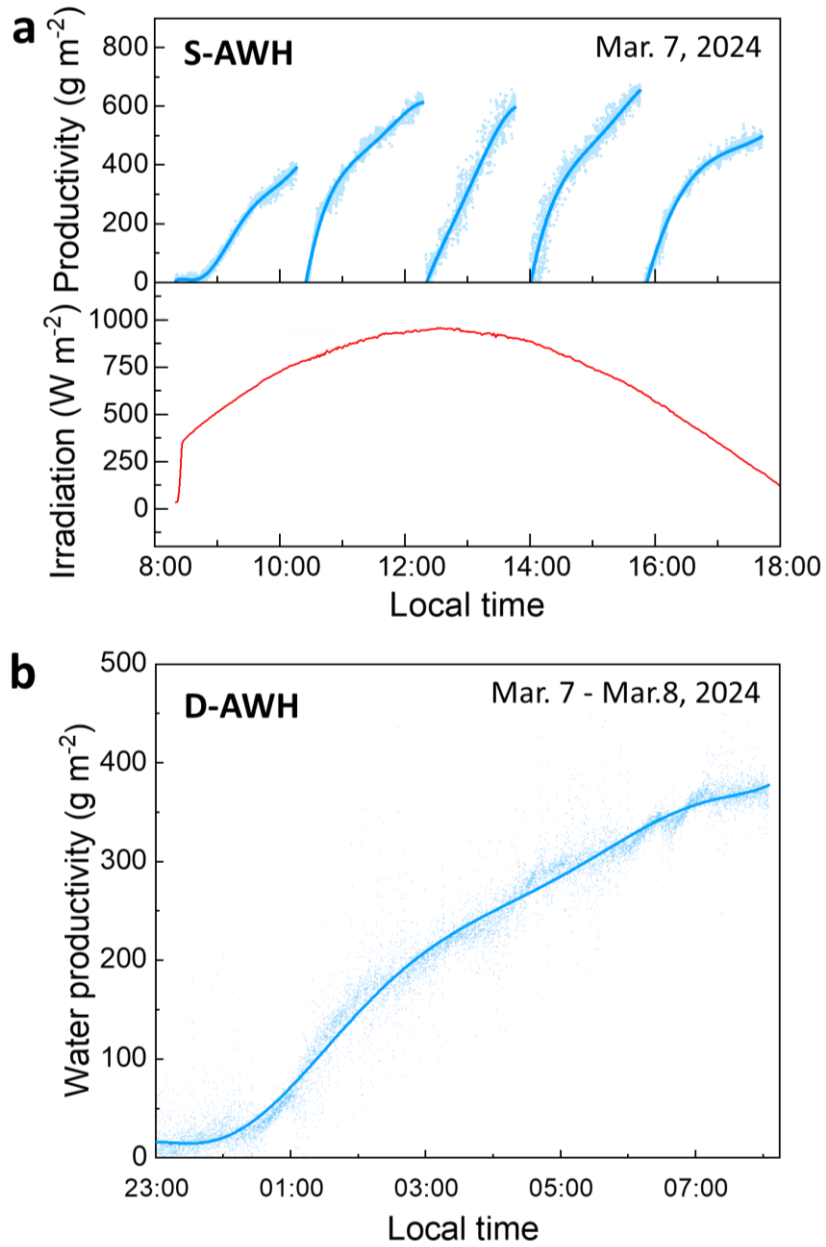


Figure S22. Water productivity of S-AWH and D-AWH on Mar. 7 - Mar. 8, 2024. in Kunming, Yunnan province, China.

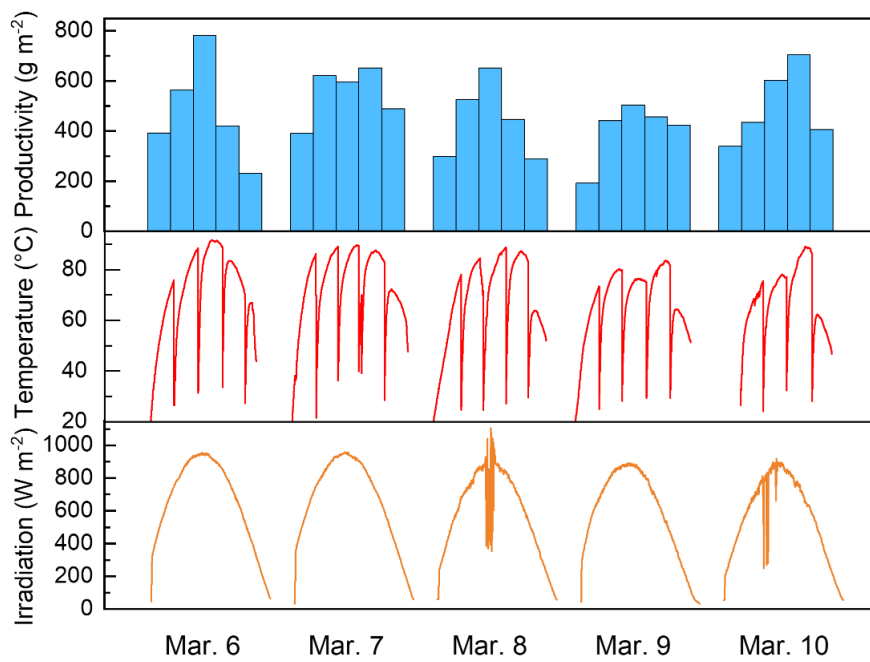


Figure S23. A five-day continuous SAWH demonstration from Mar. 6 to Mar. 10, 2024, was tested in Kunming, Yunnan province, China. Water productivity changes with the desorption temperature and solar irradiation.

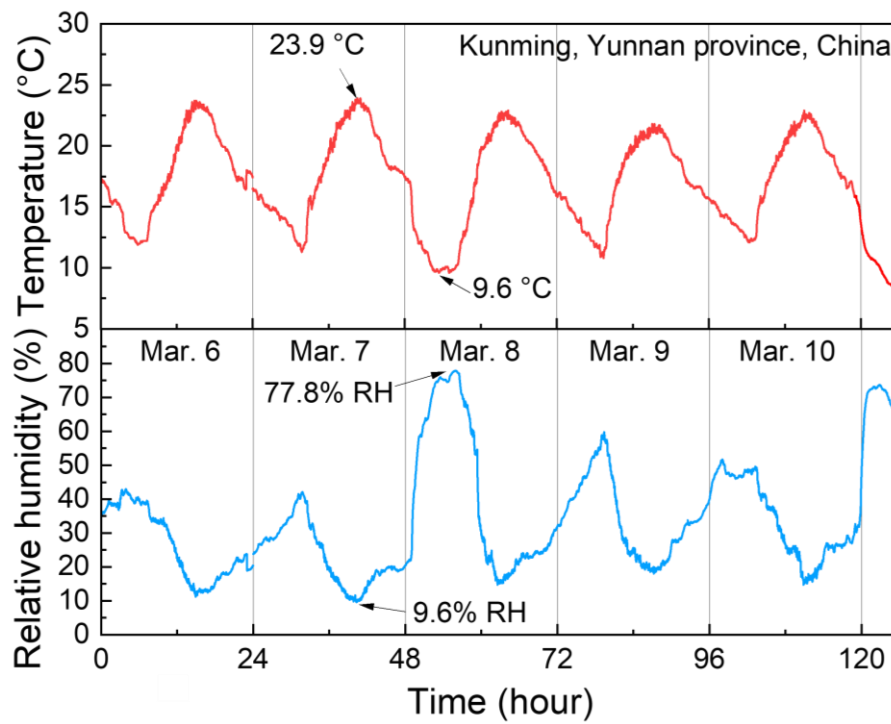


Figure S24. Temperature and relative humidity of ambient air on Mar. 6 - Mar. 10, 2024, in Kunming, Yunnan province, China.

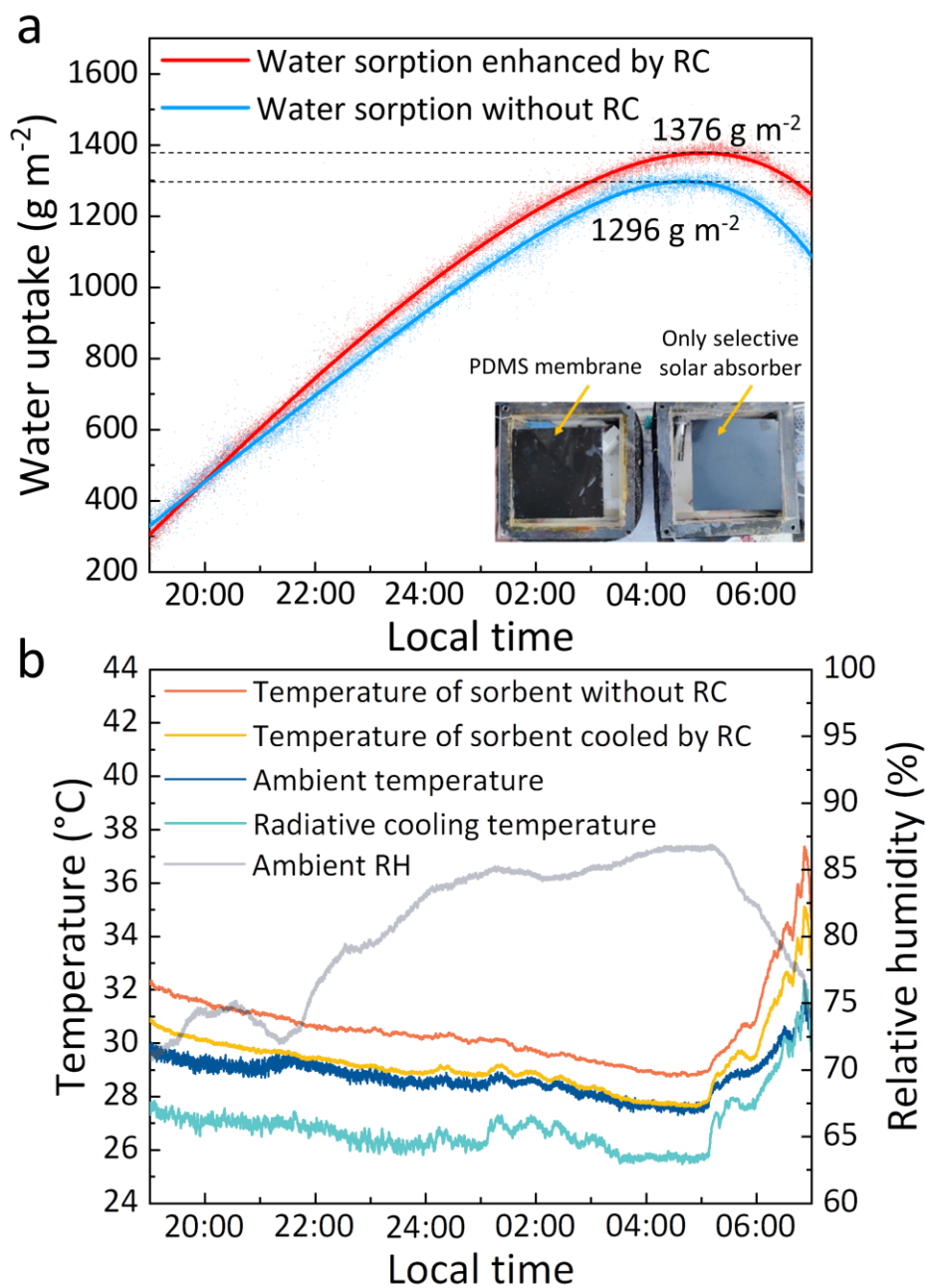


Figure S25. Comparison of dynamic water sorption of LiCl@rGO-SA with and without radiative cooling effects, tested at July 28-July 29, 2022. a, Dynamic water uptake of sorbents with and without coating PDMS membrane. b, Temperature changes of sorbents, together with local temperature and RH of air.

Table S1. The comparison of the efficiency of condensers (EOC) with different heat transfer ways in surface area, mass, and volume.

	EOC _{area} W/(m ² ·K)	EOC _{mass} W/(Kg·K)	EOC _{volume} W/(m ³ ·K)
Radiative cooling by PDMS*	181	1207	1206667
Optimized maximum natural air-cooling power by an aluminum plate-fin heat sink (13)	198	0.07	279
Optimized maximum forced air-cooling power by an aluminum plate-fin heat sink (14)	1242	34	21540

*The thickness of the PDMS membrane is selected as 150 μm, and the units of EOC for radiative cooling power are W/m², W/kg, and W/m³.

Table S2. Energy efficiency comparison of this work with other reported devices

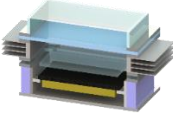

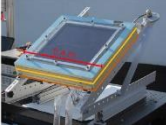
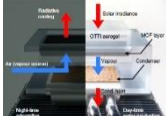
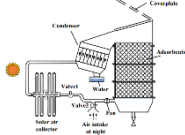
Device	Sorbent	Type of device	Relative humidity	Thermal efficiency	Reference
	LiCl@rGO-SA	Passive and discontinuous	50%	26.1%	This work
	LiCl@rGO-SA	Active and continuous	40-70%	16.1%	(1)
	AQSOA-1	Passive and discontinuous	57-68%	10.6%	(21)
	MOF-801	Passive and discontinuous	10-40%	14.0%	(22)
	ACF-LiCl	Active and discontinuous	70-90%	20.8%	(23)

Table S3. The costs of materials in the all-day AWH device

Materials	Price (\$)
Raw materials for preparing rGO	0.28
LiCl	0.46
SA	0.53
PDMS film	3.43
PE film	0.14
PET hydrophilic film	0.29
Selective solar absorber	2.86
Aluminum fins condenser	0.91
Solar reflective film	0.14
Acrylic enclosure	0.98
Insulation cotton	0.29
Acrylic glue	0.18
Sealing silicone	0.36
Total	10.85

The total price of our constructed demonstration device is approximately 10.85 \$. If consumers want a 1 L day⁻¹ water productivity, the initial investment cost of the all-day AWH device is about 296.9 \$. We would like to mention that the above price was offered by the online store, and the value can be further lower if considering the mass production of all-day AWH devices in the future.

Table S4. Techno-economic assessment of the all-day AWH device

Variable	Symbol	Unit	Value	Notes
CAPEX	Capital expenditure of the AWH device	\$ kg _{device} ⁻¹	16.32	The mass of the device includes sorbent, solar absorber, radiative cooling membrane, acrylic enclosure, insulation cotton, and other materials for sealing.
CRF	Capital recovery factor	-	0.08	The CRF is determined by system lifetime (30 years) and annual discount rate (7% per year).
OPEX _{fix}	Fixed operations and maintenance costs	\$ kg _{device} ⁻¹ year ⁻¹	0.33	The OPEX _{fix} is estimated as the 2% of CAPEX
OPEX _e	Variable operating costs associated with energy consumption	\$ L _{water} ⁻¹	0	OPEX _e is zero for the AWH device driven by solar heating and radiative cooling.
Yield	Annual water productivity per kg of device	L _{water} year ⁻¹ kg _{device} ⁻¹	15.2	The annual water productivity is calculated by daily water productivity multiplied by 365.

The levelized cost of water (LCOW) framework is calculated by the following equation,²⁴

$$\text{LCOW} = \frac{\text{CAPEX} \cdot \text{CRF} + \text{OPEX}_{\text{fix}}}{\text{Yield}} + \text{OPEX}_e \quad \text{Eq. S24}$$

where the CAPEX is the capital expenditure of the AWH device including the sorbent. CRF is the capital recovery factor. Yield is the annual water produced. OPEX_{fix} and OPEX_e are the fixed operations and maintenance costs and variable operating costs associated with energy consumption.

References

1. J. Xu, T. Li, T. Yan, S. Wu, M. Wu, J. Chao, X. Huo, P. Wang, & R. Wang. Ultrahigh solar-driven atmospheric water production enabled by scalable rapid-cycling water harvester with vertically aligned nanocomposite sorbent. *Energy and Environmental Science* **14**, 5979-5994 (2021).
2. N. Yu, R. Z. Wang, Z. S. Lu, L. W. Wang, and T. F. Ishugah. Evaluation of a three-phase sorption cycle for thermal energy storage. *Energy* **67**, 468-478 (2014).
3. X. Zheng, R. Z. Wang, T. S. Ge, and L. M. Hu. Performance study of SAPO-34 and FAPO-34 desiccants for desiccant coated heat exchanger systems. *Energy* **93**, 88-94 (2015).
4. L. G. Gordeeva, M. V. Solovyeva, A. Sapienza, and Y. I. Aristov. Potable water extraction from the atmosphere: Potential of MOFs. *Renewable Energy* **148**, 72-80 (2020).
5. H. Kim, S. Yang, S. R. Rao, S. Narayanan, E. A. Kapustin, H. Furukawa, A. S. Umans, O. M. Yaghi, and E. N. Wang. Water harvesting from air with metal-organic frameworks powered by natural sunlight. *Science* **356**, 430-434 (2017).
6. F. athieh, M. J. Kalmutzki, E. A. Kapustin, P. J. Waller, J. Yang, and O. M. Yaghi. Practical water production from desert air. *Science Advances* **4**, eaat3198 (2018).
7. J. Xu, T. Li, J. Chao, S. Wu, T. Yan, W. Li, B. Cao, and R. Wang. Efficient solar-driven water harvesting from arid air with metal-organic frameworks modified by hygroscopic salt. *Angewandte Chemie International Edition* **59**, 5202-5210 (2020).
8. R. Li, Y. Shi, M. Alsaedi, M. Wu, L. Shi, and P. Wang. Hybrid hydrogel with high water vapor harvesting capacity for deployable solar-driven atmospheric water generator. *Environmental Science & Technology* **52**, 11367-11377 (2018).
9. L. Zhou, H. Song, J. Liang, M. Singer, M. Zhou, E. Stegenburgs, N. Zhang, C. Xu, T. Ng, X. Yu, B. Ooi, and Q. Gan. A polydimethylsiloxane-coated metal structure for all-day radiative cooling. *Nature Sustainability* **2**, 718-724 (2019).
10. IR transmission spectra. <https://www.gemini.edu/observing/telescopes-and-sites/sites#Transmission>.
11. I. Haechler, H. Park, G. Schnoering, T. Gulich, M. Rohner, A. Tripathy, A. Milionis, T. M. Schutzius, and D. Poulikakos. Exploiting radiative cooling for uninterrupted 24-hour water harvesting from the atmosphere. *Science Advances* **7**, eabf3978 (2021).
12. J. J. Otten, J. P. Hellwig, and L. D. Meyers. Dietary reference intakes: the essential guide to nutrient requirements. *National Academies Press* (2006).
13. A. Bar-Cohen, M. Iyengar, and A. D. Kraus. Design of optimum plate-fin natural convective heat sinks. *Journal of Electronic Packaging* **125**, 208-216 (2003).
14. A. Bar-Cohen, and M. Iyengar. Design and optimization of air-cooled heat sinks for sustainable development. *IEEE Transactions on Components and Packaging technologies* **25**, 584-591 (2002).
15. F. B. Cortés, F. Chejne, F. Carrasco-Marín, et al. Water adsorption on zeolite 13X: comparison of the two methods based on mass spectrometry and thermogravimetry. *Adsorption* **16**, 141-146 (2010).
16. R. H. Mohammed, O. Mesalhy, M. L. Elsayed, et al. Revisiting the adsorption equilibrium equations of silica-gel/water for adsorption cooling applications. *International Journal of Refrigeration* **86**, 40-47 (2018).

17. M. V. Solovyeva, L. G. Gordeeva, T. A. Krieger, et al. MOF-801 as a promising material for adsorption cooling: Equilibrium and dynamics of water adsorption[J]. *Energy Conversion and Management* **174**, 356-363 (2018).
18. A. J. Rieth, S. Yang, E. N. Wang, et al. Record atmospheric fresh water capture and heat transfer with a material operating at the water uptake reversibility limit. *ACS Central Science* **3**, 668-672 (2017).
19. N. Hanikel, M. S. Prévot, F. Fathieh, et al. Rapid cycling and exceptional yield in a metal-organic framework water harvester. *ACS Central Science* **5**, 1699-1706 (2019).
20. N. Hanikel, X. Pei, S. Chheda, et al. Evolution of water structures in metal-organic frameworks for improved atmospheric water harvesting. *Science* **374**, 454-459 (2021).
21. A. LaPotin, Y. Zhong, L. Zhang, L. Zhao, A. Leroy, H. Kim, S. Rao, and E. N. Wang. Dual-stage atmospheric water harvesting device for scalable solar-driven water production. *Joule* **5**, 166-182 (2021).
22. H. Kim, S. R. Rao, E. A. Kapustin, L. Zhao, S. Yang, O. M. Yaghi, and E. N. Wang. Adsorption-based atmospheric water harvesting device for arid climates. *Nature Communications* **9**, 1191 (2018).
23. J. Y. Wang, J. Y. Liu, R. Z. Wang, and L. W. Wang. Experimental investigation on two solar-driven sorption-based devices to extract fresh water from atmosphere. *Applied Thermal Engineering* **127**, 1608-1616 (2017).
24. J. D. Kocher and A. K. Menon. Addressing global water stress using desalination and atmospheric water harvesting: a thermodynamic and technoeconomic perspective. *Energy & Environmental Science* **16**, 4983-4993 (2023).